Trans Indian Inst Met (2014) 67(6):935–944
DOI 10.1007/s12666-014-0420-9

TECHNICAL PAPER

TP 4819

On the Solidification of a H23 Tool Steel

Meilinda Nurbanasari · Panos Tsakiropoulos · Eric J. Palmiere

Received: 9 February 2014 / Accepted: 8 April 2014 / Published online: 13 May 2014

Abstract The H23 tool steel contains high concentration of carbide forming elements, which affect the microstructure and mechanical properties. This present study described the microstructure and mechanical properties of the as cast H23 tool steel. The steel was prepared by vacuum induction melting. The microstructural investigation used XRD and electron microscope. The nano hardness and elastic moduli of matrix and carbide were also measured. The results show that the as cast microstructure consisted of ferrite matrix and M_6C, MC and $M_{23}C_6$ carbides. The eutectic M_6C carbides had two different morphologies owing to different growth mechanisms. There was agreement between the experimental results and the calculated solidification path for the H23 tool steel regarding the presence of carbides in the microstructure. The nanohardness and elastic moduli of ferrite matrix and M_6C carbides were respectively 4.2 ± 0.2 and 10.6 ± 1.2 and 198.3 ± 10.2 and 253.5 ± 11.7 GPa.

Keywords Carbide · Phase transformation · Hardness · Electron microscopy

M. Nurbanasari (✉)
Department of Mechanical Engineering, Institut Teknologi Nasional, Jl. PHH. Mustapha 23, Bandung 40124, West Java, Indonesia
e-mail: nurbanasarimeilinda@yahoo.com; meilinda@itenas.ac.id

P. Tsakiropoulos · E. J. Palmiere
Department of Materials Science and Engineering, The University of Sheffield, Sheffield S1 3JD, UK

1 Introduction

The H23 tungsten hot work tool steel has good hot hardness and good tempering resistance up to 600 °C and is used for die casting dies with hardness 32–39 HRC [1]. Among the tungsten hot work tool steels, the H23 tool steel has the highest concentration of carbide forming elements. It is well known that carbides in tool steels play a key role in defining their mechanical properties and that their type and morphology are affected by the chemical composition of the tool steel and the solidification process [2–5] that influence the growth mechanism of primary carbides [6, 7]. The typical fishbone morphology of M_6C eutectic carbide is not affected by the chemical composition of the steel but the distance between lamellae is reduced by increasing cooling rate [3, 6]. Previous investigations tended to focus on high speed tool steel [3, 5, 6, 8–10]. To our knowledge this is the first time that the solidification microstructure of a H23 tool steel has been studied. The aim of this work was to investigate the solidification microstructure and carbide formation in a H23 tool steel. X-ray diffraction and electron microscopy were used to characterise the microstructure, which was compared with thermodynamic calculations. The analysis of microstructure included measurements of grain size, carbide volume fraction and carbide mean size. The nanohardness of the matrix and M_6C carbide and the hardness of the as cast tool steel were also measured.

2 Experimental Method

The ingots (280 × 75 × 70 mm^3) of the H23 tool steel of this study were produced using vacuum induction melting with air cooling. The mould material used was cast iron.

The chemical composition of the tool steel was determined by XRF. Samples for microstructure studies were taken from the middle top of the ingots. The Groesbeck's etchant (100 ml H_2O, 10 g NaOH, and 10 g $KMnO_4$) [11] was used with etching time 5–10 s. Optical microscopy was carried out on a MET Polyvar microscope. XRD was used for phase identification using a Siemens D5000 diffractometer and Co radiation. The samples were scanned from 2θ angles ranging from 30° through to 130°, using step size of 0.02° with a counting time 1°/min. The peaks were identified using the STOE WinXPow software program and the ICDD (International Centre for Diffraction Data) files. The SEM investigation was conducted on Inspect F and JEOL 6400 microscopes that were operated at 20 kV. The latter was equipped with EDS and INCA software for quantitative chemical analysis. Carbon extraction replicas for TEM studies were prepared using the Villella's solution (1gr picric acid, 5 ml HCl. 100 ml ethanol). Thin foils for TEM studies were produced using electrolytic jet polishing with a solution of 5 % perchloric acid, 35 % butoxyethanol and 65 % methanol [12]. The TEM studies were performed on a JEOL 2010F electron microscope equipped with EDS and operated at 200 kV.

The hardness of tool steels is not only affected by the type and volume fraction of carbides but also by the size and distribution of carbides. The Vickers hardness was measured with 10 kg load and 15 s dwell time using a CV Instrument Vickers hardness tester. Six measurements per sample were made to calculate the mean value and standard deviation. Nanohardness (H) and elastic moduli

Table 1 Chemical composition of the H23 tool steels (wt%)

C	Mn	Si	Cr	Ni	W	V	P	S	Co	Mo
0.3	0.4	0.5	12.3	0.4	12.3	1.2	0.0[illegible]	0.03	<0.02	<0.02

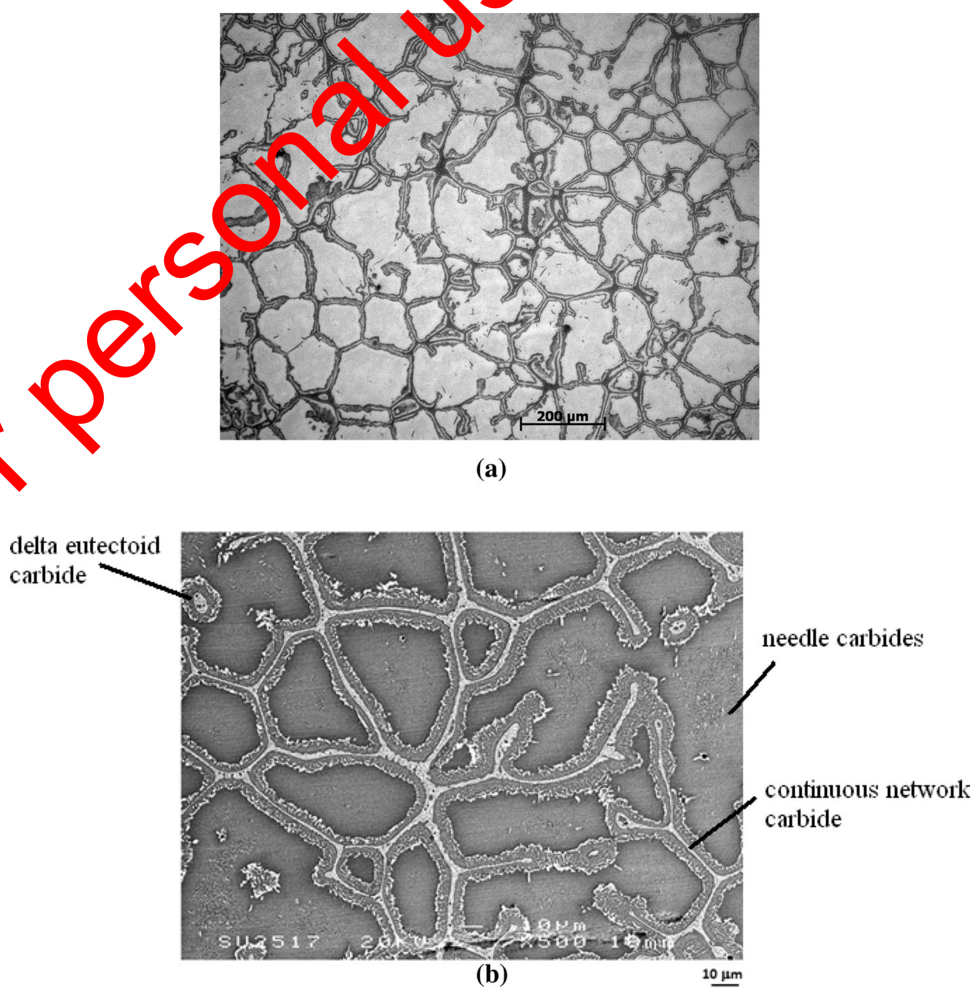

Fig. 1 Light micrograph (**a**) and SEM secondary electron image (**b**) of the as cast H23 tool steel

(E) measurements on mechanically polished samples were performed on a Triboscope (Hysitron Inc.). A standard 142.35° Berkovich indenter was employed and a load of 3,000 μN was applied with a 5 s upload, a 5 s hold and a 5 s download at constant strain rate. The recorded load versus displacement curves were analysed by the method proposed by Oliver and Pharr [13]. The grain size was measured using the mean linear intercept method [14] and the average grain size was compared with the ASTM grain size number [15]. Decolnet et al. [16] and Launeau and Robin [17] reported that the grain size can be measured using the intercept method even when the grain boundaries are partially decorated by carbides. The ThermoCalc software was used to calculate the phase diagram of the tool steel using the TCEF6 database. The experimental microstructures were compared with the ThermoCalc calculation. The average diameter and the volume fraction of the coarse carbides (V_c) were measured using ImageJ software.

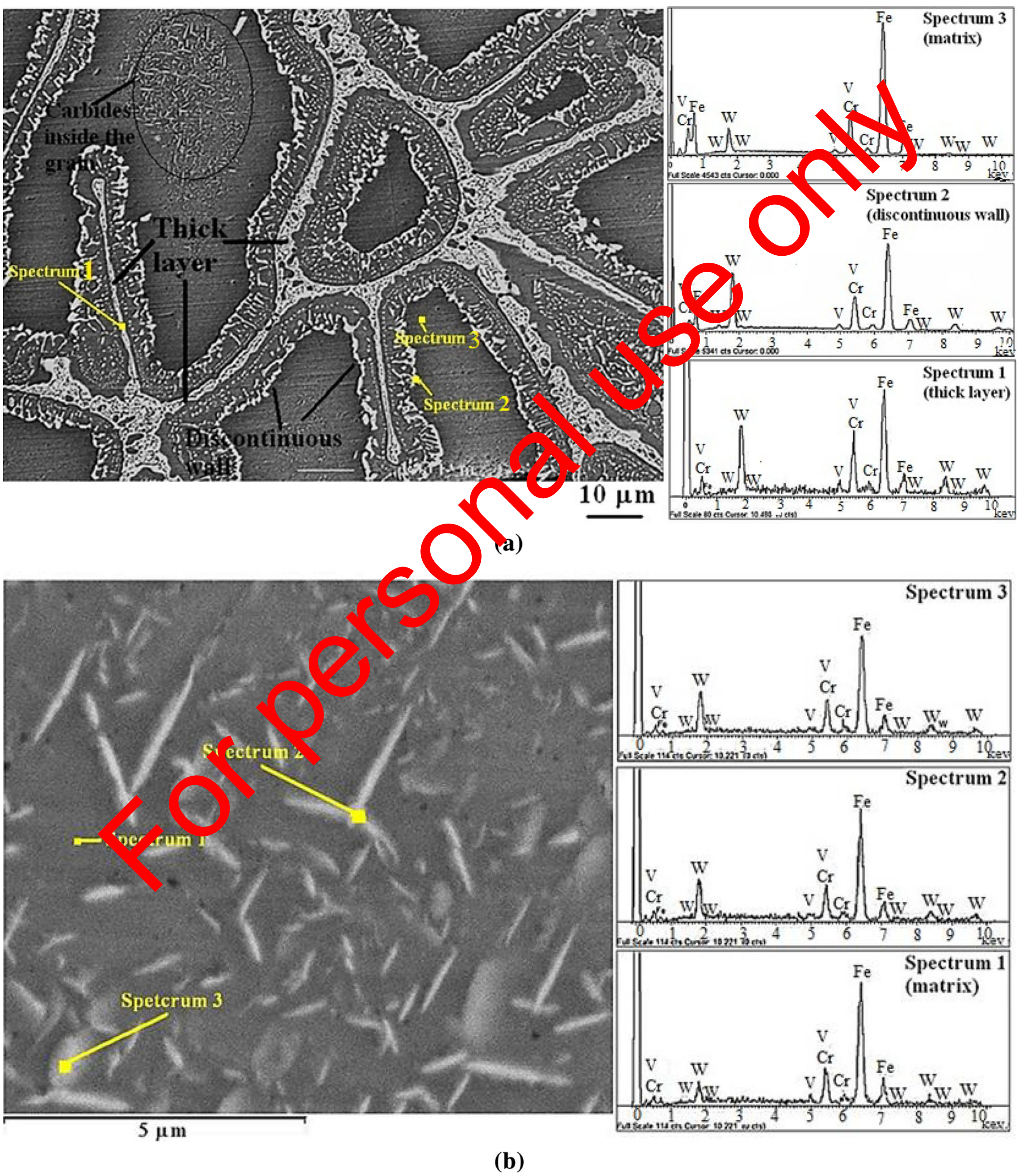

Fig. 2 SEM back scatter electron images of the as cast H23 tool steel showing the carbides along the grain boundaries (**a**) and inside the grains (**b**) and EDS spectra of the M_6C carbide and matrix

Table 2 SEM-EDS data of the M_6C carbides and matrix in the as cast H23 tool steel (wt%)

Figure	Phase	Spectrum	Element				Comment
			Fe	Cr	V	W	
2.a	Carbides in the thick layer	1	55.9	18.6	2.8	22.7	M_6C
	Carbides in the discontinuous wall	2	52.2	16.2	2.5	29.1	M_6C
	Matrix	3	79.1	13.4	0.6	7.1	α*
2.b	Carbides inside the grain	1	62.0	12.6	2.0	23.4	M_6C
		2	62.9	12.9	0.5	23.8	M_6C
		3	76.1	12.9	1.3	9.7	α*

*See Fig. 3

Note that when using the ImageJ software, the calibration of the magnification must be carried out. In this work, the optical images were converted to gray scale (type : 8 bit) and the lower and upper threshold was set to approximately 0 and 165 repectively. The analysis was done on binary images.

3 Results and Discussion

3.1 As Cast Microstructure

The chemical composition of the tool steel is given in Table 1.

Compared with the standard chemical compositions of the H23 grade tool steel, alloying elements were in the range of the AISI standard [18]. Figure 1a shows that the as cast microstructure was coarse and consisted of ferrite matrix and carbides.

The grain size of the as cast microstructure varies from 5 µm up to 200 µm and the average grain size was 84.8 ± 1.8 µm (equivalent to approximately number 4 of the estimated ASTM grain size number), which is the later dominantly affected by the cellular/dendritic features. The carbides predominantly formed a continuous network along the grain boundaries and needle carbides and delta eutectoid carbide were formed inside the grains, see Fig. 1b. Back scatter electron imaging was used to identify the type of carbide, see Fig. 2 and SEM EDS analysis of the carbide and matrix is presented in Table 2.

Figure 2 SEM back scatter electron images of the as cast H23 tool steel showing the carbides along the grain boundaries (a) and inside the grains (b) and EDS spectra of the M_6C carbide and matrix. Carbides along grain boundaries and grain interiors with significant difference in morphology exhibited white contrast. The morphology of carbides formed inside the grains was rod-like, suggesting anisotropic growth. Grain boundary carbides were thick layer carbides (skeleton) on the actual grain boundaries and carbides that formed a "discontinuous wall" around the

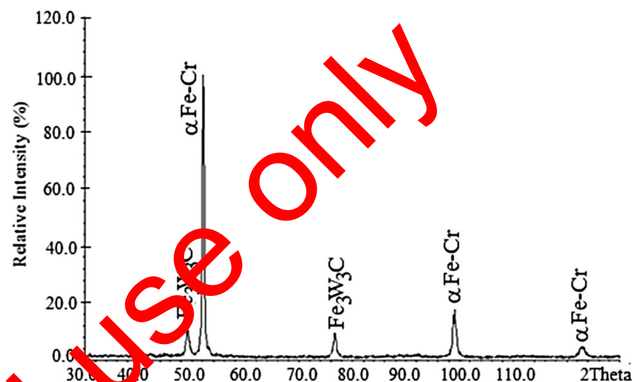

Fig. 3 X-ray diffractograms of the as cast H23 tool steel

outer edge of the eutectic colony that was formed on either side of the grain boundary.

It is well known that the M_6C carbide is W or Mo rich carbide in which Fe, Cr, V and Co may exist [1]. Figure 2 and Table 2 also show that the alloying element content of the M_6C carbides formed on the discontinuous wall (spectrum 2, in Fig. 2a) was higher than that of the M_6C carbides formed inside the grains (spectrum 1 and 2 in Fig. 2b). This was attributed to the M_6C carbides on the discontinuous wall having nucleated first on more energetically favourable site than the intragranular sites where the needle carbides formed inside the grains. Hence the size of the former carbides was bigger than that of the latter. Note that, the quantitative data in Table 2 should be considered with caution given the size of the carbides. The coarse M_6C carbide mean size was about 0.4 ± 0.1 µm and its total volume fraction was 21.5 ± 0.4 %. The mean size of the formation M_6C carbides in the as cast H23 tool steel could not be measured accurately due to the formation of continuous carbide network along the grain boundaries. The XRD (Fig. 3) confirmed the presence of ferrite matrix and Fe_3W_3C carbide in the tool steel.

The peak positions of α Fe–Cr, and M_6C (Fe_3W_3C) carbides agreed well, respectively, with the ICDD card numbers 34–396 and 41–1351. No peaks of other carbide

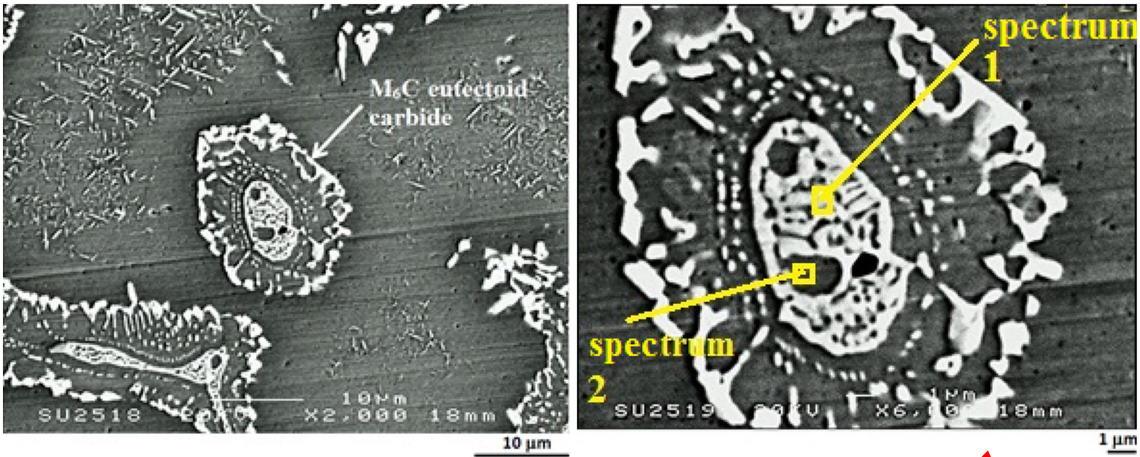

(a) Low magnification **(b)** High magnification

Fig. 4 SEM secondary electron images of the as cast H23 tool steel showing eutectoid M_6C carbides

Table 3 SEM-EDS data of the M_6C carbides and matrix in the as cast H23 tool steel (wt%)

Phase	Spectrum	Element			
		Fe	Cr	V	W
Carbide in Fig. 4	1	49.5	21.2	3.9	25.3
Matrix in Fig. 4	2	78.0	13.9	0.7	7.4

types were detected in the as cast tool steel. The carbides in Fig. 2 were identified by SEM–EDS as M_6C carbides rich in W, Cr and Fe with W the highest concentration alloying element, see Table 2. The matrix was richer in Cr than V (Table 2 and spectrum 3 in Fig. 2) as the W was consumed to form the M_6C carbides. A slight difference in the chemical composition of the M_6C carbide was suggested by spectrum 1 taken from thick layer, and spectrum 2 taken from discontinuous wall (Fig. 2). This was attributed to the shift of the composition point down a eutectic trough during the course of the eutectic reaction [3]. With respect to the M_6C carbide size, which is in the range 0.1–1.5 µm and the spatial resolution of the used EDS was almost 1 µm, there was no interference between the interaction volume and the matrix for the larger M_6C carbides (>1 µm). However, for the smaller M_6C carbides, there was interference between the interaction volume and the matrix, and thus the EDS analysis could have shifted to the matrix. The EDS result for the matrix was more accurate.

Figure 4 shows details the eutectoid M_6C carbide in the as cast tool steel and Table 3 gives SEM–EDS analysis of eutectoid M_6C carbide and matrix. The eutectoid carbide was identified as M_6C owing to its high W content. The morphology of the eutectoid carbide was of irregular shape and exhibited features that were nearly the same as for the eutectic carbide. However, the alloying element content of eutectoid M_6C carbide was higher than that of eutectic M_6C carbide due to all the major carbide forming elements being ferrite formers and soluble in ferrite and the eutectoid M_6C being the product of the delta eutectoid transformation. The presence of fine carbides was observed by TEM, as can be seen in Figs. 5 and 6. The carbide in Fig. 5 had diameter around 40 nm and was identified as MC carbide rich in V. Another carbide observed by TEM was the $M_{23}C_6$ carbide located on grain boundary, see Fig. 6. The $M_{23}C_6$ carbide was rich in Cr and Fe [1]. The MC and $M_{23}C_6$ carbides have the same crystal structure (FCC) with different lattice parameters. The lattice parameter of the $M_{23}C_6$ carbide was ~1.06 nm and the lattice parameter of the MC carbide was ~0.44 nm. The morphology of fine $M_{23}C_6$ carbide was nearly cuboid ellipsoidal with size below 80 nm in length.

3.2 Solidification Path of the H23 Tool Steel

The formation and morphology of carbides in tool steels are strongly affected by the solidification path and the chemical composition of the steel. The ThermoCalc software was used to support the microstructure studies of the cast steel. Figure 7 shows a calculated isopleth phase diagram for the H23 tool steel and solidification path that was calculated using the Scheil-Gulliver simulation by assuming that C is fast diffusing. The chemical composition of the H23 tool steel of this study is indicated by the dashed line in the calculated phase diagram in Fig. 7a.

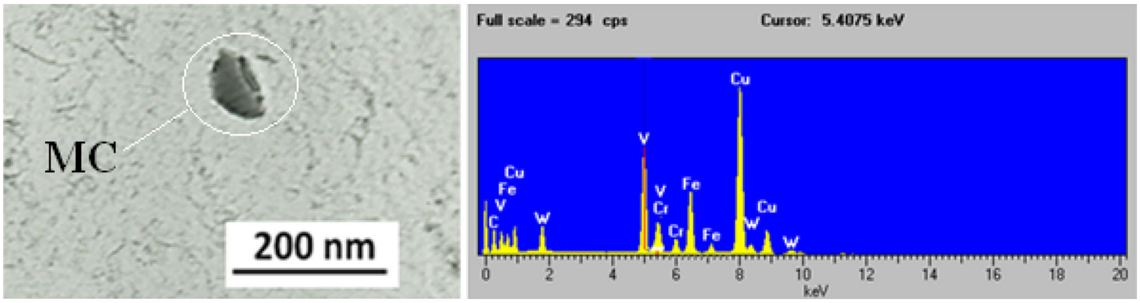

Fig. 5 A bright field TEM image from replica showing a fine MC carbide of the as cast H23 tool steel and TEM-EDS spectrum of the MC carbide. The high Cu peaks in the EDS spectrum were from the Cu grid

Fig. 6 A bright field image TEM image and EDS spectrum of the $M_{23}C_6$ carbide and selected area diffraction pattern of the $M_{23}C_6$ carbide in the as cast H23 tool steel taken from thin foil

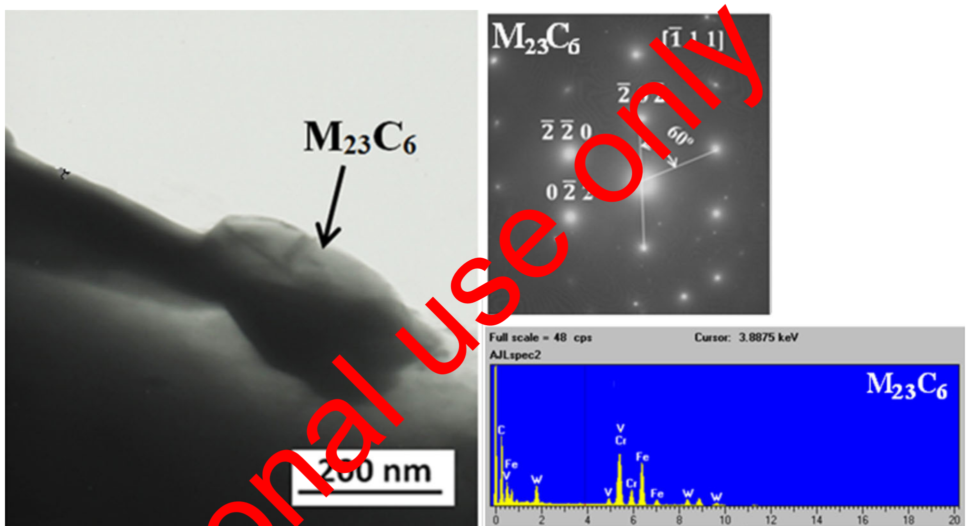

The calculated isopleth and solidification path of the H23 tool steel would suggest the following solidification stages:

(1) Stage 1 : precipitation of delta ferrite from liquid (L→δ)
At this stage delta (primary) ferrite started to crystallise from the liquid. The starting temperature of solidification was 1,476 °C.

(2) Stage 2: formation of austenite through peritectic reaction
The ending temperature of peritectic transformation was 1,280 °C. The Scheil-Gulliver diagram for the H23 tool steel in Fig. 7b shows reactions with the order:
(a) L + δ→M_6C (indicated by number 3)
(b) L + δ→M_6C + $M_{23}C_6$ (indicated by number 4)
(c) L + δ→γ + M_6C + $M_{23}C_6$ (indicated by number 5)
Therefore, the M_6C and $M_{23}C_6$ carbides crystallised at different temperatures. The peritectic reaction, which produced austenite and carbides, did not go to completion. The remaining liquid decomposed through the eutectic transformation.
The high W and Cr contents in the H23 tool steel depressed the peritectic temperature and reduced the γ phase region. As a consequence, the gap between the liquidus and peritectic temperatures was widened.

(3) Formation of carbides through eutectic reaction (L→γ + carbides).
The eutectic reaction was the last phase transformation from liquid to solid during the solidification process. The nucleation and growth of eutectic phases occurred in the remaining liquid, which was rich in C and carbide forming elements. Based on the Scheil-Gulliver simulation of the H23 tool steel, the eutectic carbides in the H23 tool steel were M_6C, $M_{23}C_6$ and MC and formed in the temperature range 1,295–1,225 °C. The M_6C was the first eutectic carbide that formed at 1,295 °C, followed by the formation of $M_{23}C_6$ at 1,280 °C and MC at 1,225 °C.

As discussed before, the differences in carbide morphology imply different growth mechanisms for the

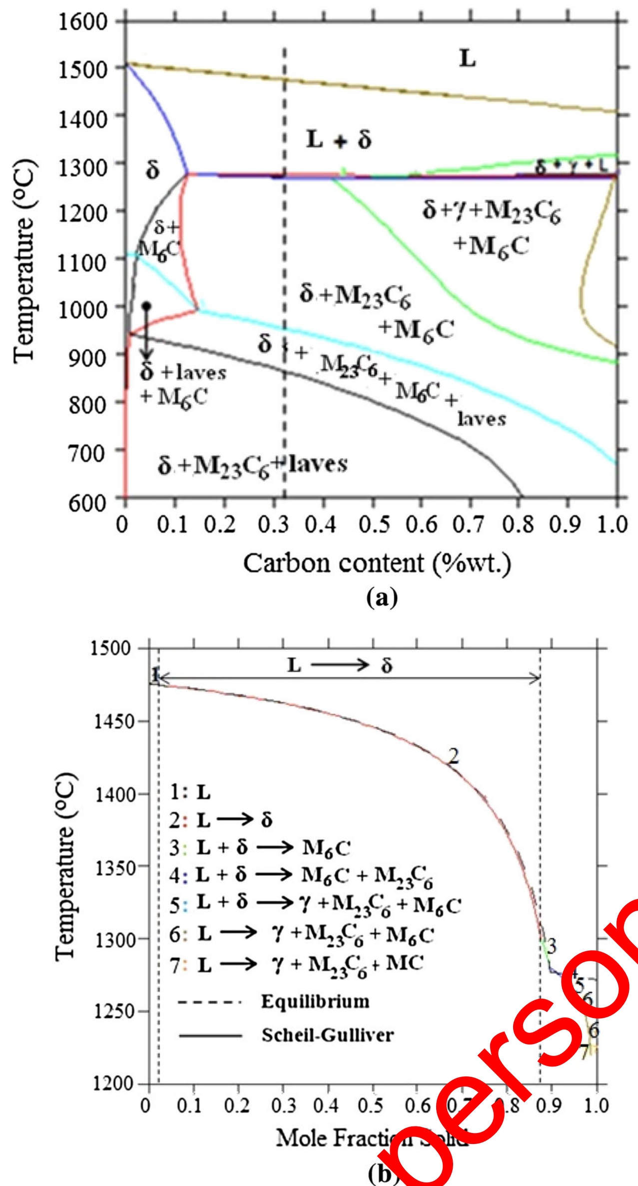

Fig. 7 Calculated isopleth (a) and solidification path (b) of the investigated H23 tool steel

discontinuous wall carbide, the skeleton carbide, the carbides inside the grains and the delta eutectoid carbides. On the basis of the aforementioned solidification path and the as cast microstructure, it is suggested that the formation and growth of primary carbides (in the metallurgy of tool steels primary carbides are those formed upon solidification) in the H23 tool steel occurred as shown in the schematic diagram in Fig. 8. Figure 8 can be as explained as follows:

(1) Stage 1: L→δ
The solidification started with the formation of primary δ ferrite at 1,476 °C.

(2) Stage 2: L + δ→M_6C + γ
As the temperature decreased, the peritectic reaction occurred. Due to the high content of carbide forming elements in the tool steel, the M_6C carbides formed first through the peritectic reaction and then austenite. The as cast microstructure of the H23 tool steel suggested that there were two different sites of M_6C carbide formation. First, the M_6C carbide was the leading phase of the peritectic transformation [6] and nucleated on the melt/δ ferrite interface to form discontinuous wall and thickened as solidification progressed. Second, because of the high content of carbide forming elements the melt/ferrite interface could no longer accommodate all the carbide forming elements and M_6C carbides nucleated independently in the less favourable intragranular sites of δ ferrite. Hence, at the end of the solidification process the M_6C carbides were distributed not only at the grain boundaries but also inside the grains. The M_6C carbides, which formed first, grew cooperatively with the austenite that formed from the peritectic transformation. The peritectic austenite grew and covered the δ ferrite and M_6C carbides.

(3) Stage 3: L→γ + M_6C
The peritectic reaction did not go to completion leaving the primary delta ferrite in the dendrite cores. This and the fact that the austenite formed a continuous shell around δ ferrite meant that further transformation was possible in the solid state [3, 5]. The remaining interdendritic liquid decomposed into a eutectic mixture of austenite and carbides. The eutectic transformation started at 1,295 °C with the M_6C carbide being the leading phase of the eutectic transformation. The M_6C carbides nucleated on the surface of the peritectic austenite. The as cast microstructure in Fig. 2a shows that the morphology of carbides formed along the grain boundary was a skeleton shape with characteristic midplane and regularly spaced lamellae.

(4) The peritectic γ continued to grow in the direction of δ ferrite. The eutectic M_6C carbides grew simultaneously, and connected with others [6] and finally formed thick layer (skeleton) of M_6C carbides. Fischmeister et al. [3] observed that thickening of the lamellae towards the end of solidification of the interdendritic melt may, more or less, close the interlamellar gaps often forming a continuous coating on the metal dendrites. When the interdendritic melt area was big enough, from both sides of the eutectic M_6C carbides the skeletons grew out to form a secondary axis [6], and as a result the thick layer of the M_6C carbides became bigger. The high W content in the H23 tool steel must have played an important role in the

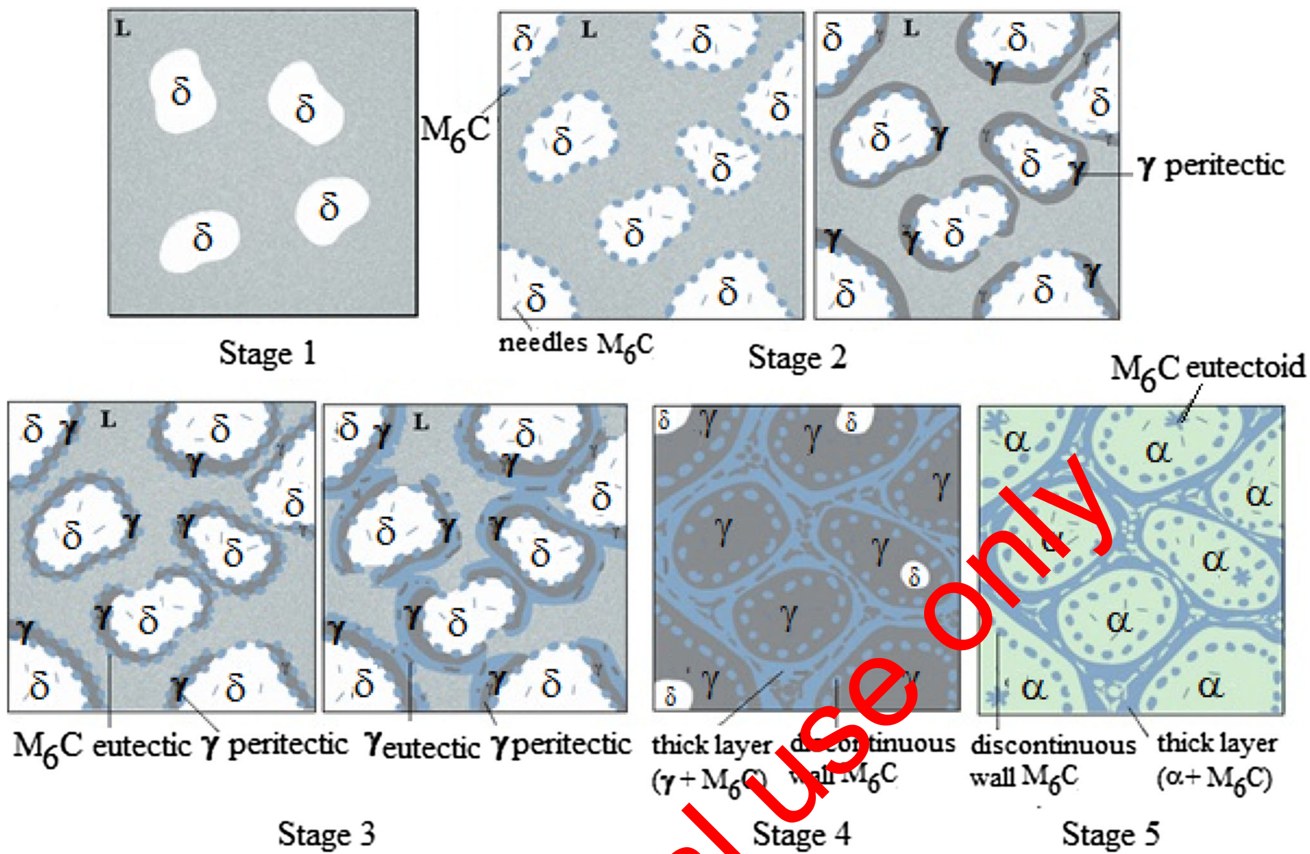

Fig. 8 Schematic showing solidification stages of the H23 tool steel

formation of carbides. Kim et al. [19] reported that V additions in a high speed steel accelerated the eutectic reaction forming M_6C carbides. The eutectic transformation terminated before the peritectic transformation and thus, there was residual delta ferrite [4].

(5) Stage 5: Formation of delta eutectoid M_6C carbides via eutectoid transformation. Kagawa and Okamoto [20] and Galda and Kral [21] reported that high W and Cr contents in steels depressed the peritectic reaction temperature. Thus, the H23 tool steel had a wide temperature range for delta (primary) ferrite crystallisation and caused delta ferrite to remain in the dendrite cores after the peritectic transformation. In this stage, the δ ferrite core was separated from the melt by wall of peritectic γ. Since the transformation is diffusion controlled, during the subsequent solidification the unconsumed delta ferrite in the dendrite cores transformed to austenite and carbide below the solidus temperature through the eutectoid transformation $\delta \rightarrow \gamma +$ carbides (known as delta eutectoid reaction [5]) and upon further cooling to room temperature the austenite transformed to ferrite. The eutectoid transformation consumed a large quantity of C and as the delta ferrite is a C poor phase, the C could only be supplied by the C rich remaining liquid [6]. Carbon must diffuse to the core through the peritectic austenite region. The substitutional alloying elements have much lower diffusion rates than C and as they had no time to diffuse to the delta ferrite in the dendrite core they segregated in the delta ferrite/austenite interface. Hence, precipitation of eutectoid carbides occurred at the austenite/delta-ferrite interface to accommodate the available carbide forming elements, which existed in the high temperature ferrite following the delta-eutectoid reaction. In the absence of the delta eutectoid carbide, as was observed in some areas, see Fig. 2b, the peritectic austenite covered part of the delta ferrite and thus, both phases were in contact with the melt that supplied the alloying components, allowing the δ ferrite to transform completely to austenite [4].

In summary, the experimental results showed that the as cast microstructure consisted of ferrite, M_6C and fine MC and $M_{23}C_6$ carbides. Comparison between the calculated solidification path and experimental results shows agreement regarding the formation of the M_6C, MC and $M_{23}C_6$ carbides.

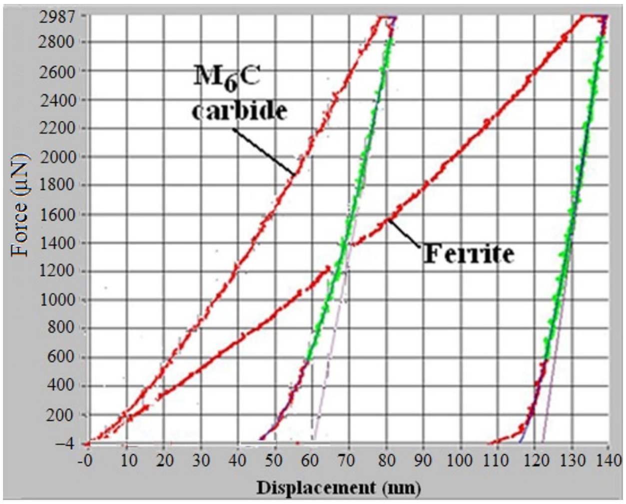

Fig. 9 Superimposed of curves of load versus displacement of ferrite and carbide

3.3 As Cast Hardness

The bulk hardness of the cast H23 tool steel was 355 ± 4 HV and was about 100 HV lower than that of a cast hot forging die steel with similar C and V content [22]. Nano indentation was performed to measure the hardness of ferrite matrix and carbide. In the Vickers hardness test, the hardness is calculated from the dimensions of the plastic indentation diagonal. In nano-indentation the hardness and elastic modulus are calculated from the load versus displacement curve recorded during indenting. First the topographic image from the specimen surface was obtained in AFM mode and then the indenting was performed. The indentations were observed in the AFM image and thus were identified as corresponding to matrix or carbide or the carbide/matrix interface. Only indentation in the bulk of carbide and matrix were used to calculate the average hardness and elastic moduli values. Figure 9 shows the load versus displacement curves from the two phases.

The plastic indentation size was larger for the matrix compared with the carbide, which indicated a higher hardness for the latter. The two phases were characterised by different load versus displacement curves, with larger displacement for the softer matrix compared with the harder carbide (see Fig. 9). Using the Oliver and Pharr method [13], the hardness H of each phase was determined from the actual contact area A from $H = F_{max}/A$ where F_{max} is the maximum load and the modulus of elasticity E of each phase was determined from the measured reduced modulus E_r from $1/E_r = [(1-\nu^2_{indenter})/E_{indenter}] + [(1-\nu^2_{phase})/E_{phase}]$ where ν denotes Poisson's ratio. The nano-hardness and moduli of elasticity of ferrite and M_6C carbide respectively were 4.2 ± 0.2 GPa and 10.6 ± 1.2 GPa and 198.3 ± 10.2 GPa (for ν = 0.36) and 253.5 ± 11.7 GPa (for ν = 0.3) or 248.5 GPa ± 11.6 (for ν = 0.19). Compared with data in the literature [23], the average nano-hardness and modulus of elasticity of the M_6C carbide in this study were slightly lower. The nano-hardness of ferrite was also slightly lower than that reported (4.8 ± 0.2 GPa) by Funermont et al. [24] for a steel with 0.3 wt% C.

Nano-size MC and $M_{23}C_6$ carbides were found by TEM. The latter were at the grain boundary of ferrite grains. The typical hardness values of $M_{23}C_6$ and MC carbides respectively are ~1000–1100 HV and 1881 HV, significantly higher compared with reported values for the hardness of ferrite in steels of different compositions [24–27]. In this work, the load versus displacement curves for bulk ferrite did not show any evidence of the indenter encountering another hard phase; thus the aforementioned average value of nano-hardness of 4.2 GPa is that of ferrite in the as cast H23 tool steel of this study. Differences in hardness values of ferrite and carbide between different grains are attributed to intrinsic differences of each grain such as crystallographic orientation and dislocation density and work hardened grains in the near surface region owing to the mechanical polishing used for specimen preparation, to not knowing the depth of the grain below the surface (in other words even a shallow indent could have sensed another phase) and even to slight variations in surface roughness.

4 Conclusions

In this work the solidification microstructure of a vacuum induction melted H23 tool steel was studied. The conclusions of the research were as follows:

(1) Two different morphologies of peritectic M_6C carbides were observed by SEM. The M_6C carbides located inside the grains had a rod like morphology and carbide that formed a "discontinuous wall" of carbides around the outer edge of the eutectic colony had an irregular morphology. Grain boundary M_6C eutectic carbides were thick layer carbides (skeleton) on the grain boundary. Eutectoid M_6C carbides formed inside some grains and their features were nearly the same as for the eutectic carbide.

(2) Fine MC and $M_{23}C_6$ carbides were observed only by TEM. The $M_{23}C_6$ were formed on the grain boundary.

(3) The calculated solidification path of the H23 tool steel was in agreement with the solidification microstructure.

(4) The nanohardness and elastic moduli of ferrite matrix and M_6C carbides were respectively 4.2 ± 0.2 GPa and 10.6 ± 1.2 GPa and 198.3 ± 10.2 GPa and 253.5 ± 11.7 GPa.

Acknowledgments The author (MN) gratefully acknowledge to the Directorate General of Higher Education, Indonesian Government and the Institut Teknologi Nasional (Itenas), Bandung for their financial support.

References

1. Roberts G A, Krauss G, Kennedy R L, *Tool Steels*, ASM International, Ohio, (1998).
2. Boccalini M, Goldenstein H, *Int Mater Rev* **46** (2001) 92.
3. Fischmeister H F, Riedl R, Karagöz S, *Metall Trans A* **20A** (1989) 2133.
4. Nizhnikovskaya P F, Kalinushkin E P, Snagovskii L M, Demchenko G F, *Metal Sci Heat Treat* **24** (1982) 777.
5. Barkalow R H, Kraft R W, Goldstein J I, *Metall Mater Trans B* **3** (1972) 919.
6. Peidao D, Gongqi S, Shouze Z, *Mater Charact* **29** (1992) 15.
7. Peidao D, Gongqi S, Shouze Z, *Acta Metall Sin (English Edn)*, **4** (1991) 165.
8. Rüssel M, Krüger L, Martin S, Kreuzer W, *Eng Fract Mech* **99** (2013) 278.
9. Kąc S, Kusiński J, *Mater Chem Phys* **81** (2003) 510.
10. Kheirandish S, Noorian A, *J Iron Steel Res Int* **15** (2008) 61.
11. Voort G F V, Metallography: ASM Metals Handbook: Metallography and Microstructures, ASM International, Ohio, (2004) 257.
12. Voort G F V, Metallography: Principles and Practice, ASM International, Ohio, (1999).
13. Oliver W C, Pharr G M, *Mater Res* **7** (1992) 1564.
14. Higginson R L, Sellars C M, Worked Examples in Quantitative Metallography, Maney Publishing, London, (2003).
15. ASTM Standard E113, Standard Test Methods for Determining Average Grain Size, Annual Book of ASTM Standard vol 03.01, American Society for Testing Materials, Philadelphia, (1999).
16. DeColnet L, Pirard E, Tchuindjang J T, Lecomite-Beckers J, Gfhiri R, Boeraeve P, Cescotto S, Proc. of the Materials Structure and Micromechanic of Fracture-3 Int Conf, Brno, (2001) 710.
17. Launeau P, *Tectonophys* **267** (1996) 91.
18. Campbell F C, Elements of Metallurgy and Engineering Alloys, ASM International, Ohio, (2008).
19. Kim C, Kim Y, Park J, Lee S, Kim N, Yang J, *Metall Mater Trans A*, **36** (2005) 87.
20. Kagawa A, Okamoto T, *Mater Sci Tech* **2** (1986) 997.
21. Galda E J, Kraft R W, *Metall Trans B* **5** (1974) 1727.
22. Min-xian W, Shu-qi W, Lan W, Xiang-hong C, Kang-min C, *J Iron Steel Res Int* **19** (2012) 50.
23. Schmauder S, Micromechanics and Nanosimulation of Metals and Composites: Advanced Methods and Theoritical Concepts, Springer-Verlag, Berlin, 2009.
24. Funermont Q, Kempf M, Jacques P J, Goken M, Delanay F, *Mater Sci Eng A*, **328** (2002) 26.
25. Choi Y, Choo W Y, Kwon D, *Scr Mater* **45** (2001) 1401.
26. Choi B W, Seo D H, Jang J, *J Met Mater Int* **15** (2009) 373.
27. Delincé M, Jacques P J, Pardoen, *Acta Mater* **54** (2006) 3395.